

Bandlike electrical transport in $\text{Pr}_{1-x}\text{Ca}_x\text{MnO}_3$ manganitesL. S. Kadyrov,^{1,2} T. Zhang,³ E. S. Zhukova,^{1,2,4} V. B. Anzin,^{1,2} V. G. Trotsenko,^{5,6} V. I. Torgashev,⁵ M. Dressel,⁴ and B. P. Gorshunov^{1,2,4,*}¹*Moscow Institute of Physics and Technology, Dolgoprudny, Moscow Region 141700, Russia*²*A. M. Prokhorov General Physics Institute, RAS, Moscow 119991, Russia*³*Key Laboratory of Materials Physics, Institute of Solid State Physics, Chinese Academy of Sciences, Hefei 230031, People's Republic of China*⁴*1. Physikalisches Institut, Universität Stuttgart, D-70569 Stuttgart, Germany*⁵*Faculty of Physics, Southern Federal University, 344090 Rostov-on-Don, Russia*⁶*Laboratory of Condensed Matter Physics, University of Picardy, F-80039 Amiens Cedex, France*

(Received 31 March 2016; published 16 May 2016)

The conductivity and dielectric permittivity spectra of polycrystalline manganites $\text{Pr}_{1-x}\text{Ca}_x\text{MnO}_3$ with $x = 0.3, 0.4,$ and 0.5 have been measured in a broad frequency range ($5\text{--}3000\text{ cm}^{-1}$) down to low temperatures. From the dispersion analysis the existence of a Drude component can be established that is associated with small polarons coherently moving within a band several meV wide. The temperature-dependent conductivity shows an activated behavior with an activation energy of approximately 165 meV above 170 K and 4.8 meV below 120 K. The change in the activation energy is assigned to the onset of magnetic order at 120 K. In all three samples an absorption band is discovered at $40\text{--}60\text{ cm}^{-1}$ that is associated with the transition between Stark-split Pr^{3+} electron states which gain optical activity due to coupling to acoustical phonons.

DOI: [10.1103/PhysRevB.93.184303](https://doi.org/10.1103/PhysRevB.93.184303)**I. INTRODUCTION**

The rich family of perovskite mixed-valence manganites $\text{RE}_{1-x}\text{A}_x\text{MnO}_3$ ($\text{RE} = \text{rare earth}, \text{A} = \text{alkaline-earth element}$) is in the center of attention and activity of researchers due to the variety of exciting phenomena that result from the unique presence of comparably strong order parameters describing charge, spin, phonon, and orbital interactions. The dynamic competition of corresponding phases produces complex phase diagrams of the compounds [1–3]. External stimuli, such as magnetic or electric fields, pressure, mechanical strain, current injection, and electromagnetic irradiation, can easily switch between the phases [4–7], making manganites attractive for various applications in electronics, spintronics, etc. At the same time, it turned out to be extremely challenging and rewarding to explore the underlying physics, and to elucidate the origin of various ground states and of the mechanisms of phase transitions between these states. An effective way to get insight into the physical properties of manganites is the spectroscopic study of their electrical conductivity since the dynamics of itinerant charge carriers is strongly affected by the magnetic, structural, and orbital states in the materials. It has been suggested [8] that polaronic charge carriers are of importance. Both small and large polarons can be identified and discriminated by optical spectroscopy, for example, according to the shape of the polaronic excitation band in the midinfrared range [9,10]. The detailed mechanisms of their dc and low-frequency conduction, however, are still under discussion. Along with observations of thermally activated polaronic hopping transport [11,12], other interpretations of the temperature-frequency dependences of the conductivity are suggested, considering metalliclike ferromagnetic inclusions in the insulating paramagnetic matrix [13], magnon scattering

[14], or the ac response of polarons revealing the well-known universalities of disordered solids—the universal dielectric response and nearly constant loss [15]. There are also strong indications towards collective effects within the polaronic condensate that can lead to coherent bandlike conduction [16,17], polaron order-disorder (solid-to-liquid) transitions [11], phase transitions associated with local spontaneous electric polarization [18], or charge-density wave instability [19–22]. Besides the fundamental complexity of the transport phenomena, their studies are also complicated by purely experimental difficulties such as the quality of crystalline, ceramic, or thin film samples, and by extrinsic contributions from grain boundaries and/or interfaces at the contacts used in dc, ac, and dielectric measurements [12,13,15,23,24].

In this paper, we present our results based on broadband dielectric spectroscopy used to study systematically the conductivity mechanisms of the colossal magnetoresistant manganite $\text{Pr}_{1-x}\text{Ca}_x\text{MnO}_3$ ($0.3 < x < 0.5$), a member of the family that has a relatively narrow one-electron band, thus showing insulating behavior over the whole range of doping levels x [23]. The compound undergoes a charge/orbital ordering transition below 220–240 K, followed by a transition to an antiferromagnetic phase at 140–180 K (depending on x), and finally to a canted antiferromagnetic insulating phase at even lower temperatures [25–27]. We have performed contactless measurements of the dynamical conductivity $\sigma(\nu)$ and dielectric permittivity $\varepsilon_1(\nu)$ (real part) and $\varepsilon_2(\nu)$ (imaginary part) at frequencies $\nu = 5\text{--}3000\text{ cm}^{-1}$ with the main emphasis on the terahertz (THz) frequency range, below 100 cm^{-1} , where the response of charge carriers is not bleared by phonon absorption.

II. EXPERIMENT

Polycrystalline $\text{Pr}_{1-x}\text{Ca}_x\text{MnO}_3$ (PCMO) samples with $x = 0.3, 0.35, 0.4, 0.45,$ and 0.5 were synthesized by a standard

*Corresponding author: bpgorshunov@gmail.com

solid-state ceramic technique [28]. Stoichiometric amounts of high-purity Pr_6O_{11} , CaCO_3 , and MnCO_3 were weighed out and intimately mixed in an agate mortar and pestle. The reactants were tempered in air at 1050, 1150, and 1350 °C, respectively, for 20 h with regrinding between heating. Finally, the tempered powder was pressed into pellets, and heated at temperatures varying from 1360 to 1450 °C for 20 h according to the doping level x . Powder x-ray diffraction measurements were made on the Bruker D8-Advance diffractometer (*Bruker AXS*, Germany) using $\text{Cu } K\alpha$ radiation $\lambda = 1.54056 \text{ \AA}$ at room temperature. As one can see from Fig. 1, the observed x-ray diffraction data of all samples are well described by the $Pnma$ space group without any secondary or impurity phases.

At terahertz frequencies, 5 up to 50–60 cm^{-1} , the $\sigma(\nu)$ and $\epsilon_{1,2}(\nu)$ spectra were measured using a cw spectrometer based on monochromatic and frequency tunable radiation sources [backward-wave oscillators (BWOs)] [29] and a pulsed time-domain spectrometer (TDS) of the Menlo Systems type. Both spectrometers operate in the transmission mode and allow for a direct determination of the spectra, without employing a Kramers-Kronig analysis. For such measurements, plane-

parallel samples of thicknesses $d \approx 200 \mu\text{m}$ and diameter $\approx 1 \text{ cm}$ were prepared and polished. In the experiment, the complex THz transmission coefficient $\text{Tr}(\nu) \exp[i\varphi(\nu)]$, with amplitude $\text{Tr}(\nu)$ and phase $\varphi(\nu)$, of the plane samples is measured in a quasi-optical arrangement (terahertz beam propagating in free space). In the BWO spectrometer, the spectra $\text{Tr}(\nu)$ are determined from the ratio of the intensity passed through the sample that covers the aperture to that passed through the empty aperture. To measure the phase shift, the Mach-Zehnder interferometric scheme is used with the sample placed in one of its arms. An electronically controlled movable mirror in the second (reference) arm maintains the interferometer in the condition of a minimal signal at the detector. The shift of this mirror Δx that is caused by introducing into the THz beam of the studied sample allows for the determination of the phase shift $\varphi(\nu) = 2\pi(\Delta x + d)\nu$ [29]. In the TDS spectrometer both the amplitude and phase of the transmission coefficient are determined by the Fourier transformation of the electric field of a picosecond pulse propagated through the sample and through the empty aperture, thus recovering the frequency-domain “image” of

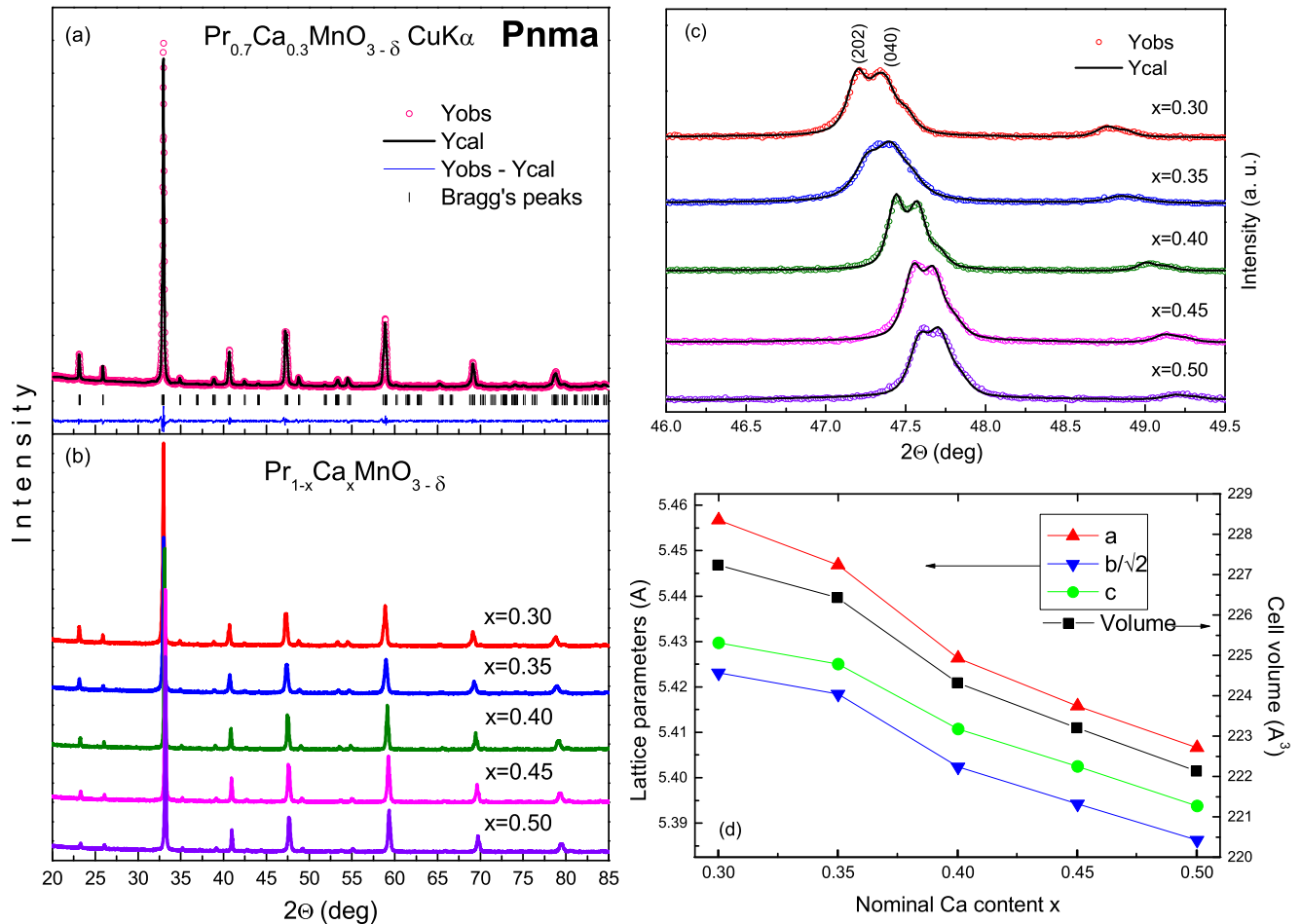


FIG. 1. X-ray powder diffraction pattern for $\text{Pr}_{1-x}\text{Ca}_x\text{MnO}_3$ ($\text{Cu } K\alpha$). (a) Profile of Rietveld refinements of $\text{Pr}_{0.7}\text{Ca}_{0.3}\text{MnO}_3$. The observed (circles), calculated (solid line), and difference (bottom line) profiles are shown. The vertical bars show the peak positions of the reflexes. (b) The diffraction patterns of $\text{Pr}_{1-x}\text{Ca}_x\text{MnO}_3$ with $x = 0.3, 0.35, 0.4, 0.45$, and 0.5 are indexed in the orthorhombic space group $Pnma$. (c) High-resolution x-ray powder diffraction of $\text{Pr}_{1-x}\text{Ca}_x\text{MnO}_3$ in the $47^\circ < 2\theta < 48^\circ$ region. (d) The lattice parameters and the unit cell volume of the $\text{Pr}_{1-x}\text{Ca}_x\text{MnO}_3$ solid solution samples. The values of the lattice parameter b were divided by a factor $2^{1/2}$. Symbols represent experimental data. The error bars are smaller than the symbol size in all cases.

the pulse. In both spectrometers, after the spectra of the two quantities, $\text{Tr}(\nu)$ and phase $\varphi(\nu)$, are determined, the spectra of any pair of optical constants (real and imaginary parts of the refractive index, dielectric permittivity, optical conductivity, etc.) are calculated using standard Fresnel expressions for the complex transmission coefficient of a plane-parallel slab [30], by solving a corresponding set of two nonlinear equations. All measurements and the determination of optical constant spectra are fully automated and controlled by a computer. We note that with the sample thicknesses of about $200 \mu\text{m}$ we were able to perform reliable transmissivity measurements only below $\approx 200 \text{ K}$, where the samples were transparent enough. In the infrared (IR) range, the spectra of reflection coefficients were measured with the help of a standard Fourier-transform spectrometer Vertex 80 V by comparing the intensity reflected by the samples with that reflected by gold or aluminum reference mirrors. The broadband THz-IR spectra of $\sigma(\nu)$, $\varepsilon_{1,2}(\nu)$, were obtained by merging the directly measured THz spectra with these determined by the model dispersion analysis of the IR reflectivity spectra. This model analysis is described in more detail in the next section. The room-temperature conductivity spectra of the samples at frequencies up to 3000 cm^{-1} were obtained via a Kramers-Kronig analysis of the reflectivity spectrum.

All measurements were performed at temperatures between 10 and 300 K using homemade optical cryostats with Mylar and polyethylene windows in the THz and IR ranges, respectively.

III. RESULTS AND ANALYSIS

The experimental and calculated x-ray diffraction (XRD) patterns for the sample $\text{Pr}_{0.7}\text{Ca}_{0.3}\text{MnO}_3$ are shown in Fig. 1(a). All the reflection peaks of the profile were determined and categorized by an orthorhombic structure with space group $Pnma$ from the Rietveld analysis of the XRD data using the FULLPROF suite. X-ray diffraction patterns of $\text{Pr}_{1-x}\text{Ca}_x\text{MnO}_3$ powder are presented in Fig. 1(b). It presents a single phase for all compounds. It is found that all samples also belong to the orthorhombic structure and the space group is $Pnma$ (No. 62). The intensity of the first reflections (101) and (020) in the 2θ range 23° – 24° is decreased with increasing Ca concentration. This means that the distortion of the perovskite structure is decreased [31]. It should be noted that, with an increase in the concentration Ca, the positions of the Bragg peaks are shifted toward higher diffraction angles [shown in Fig. 1(c)], which correspond to a lattice compression. It is clear from Fig. 1(d) that the lattice parameters and the volumes of the unit cells decrease upon substituting trivalent cation Pr^{3+} with divalent cation Ca^{2+} . Although the ionic radius of Pr^{3+} is smaller than in Ca^{2+} ions, the observed behavior might be attributed to the growth of the number of Mn^{4+} ions having a smaller radius than Mn^{3+} since the amount of Ca concentration increases the hole doping in PCMO [32].

The upper frames of Figs. 2–4 show the reflectivity spectra $R(\nu)$ of the $\text{Pr}_{1-x}\text{Ca}_x\text{MnO}_3$, $x = 0.3, 0.4, 0.5$ samples measured in the IR range, together with the reflectivity data calculated from directly determined THz spectra $\sigma(\nu)$ and $\varepsilon_1(\nu)$ according to Fresnel formulas. Above 100 cm^{-1} , typical features due to phonon resonances are clearly seen in the

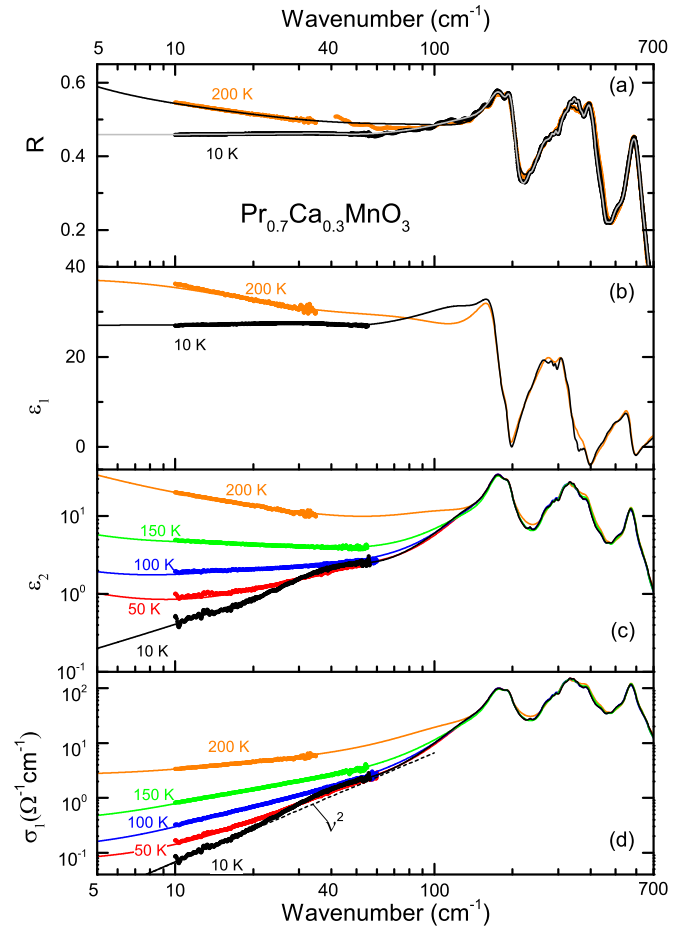


FIG. 2. Spectra of the (a) reflection coefficient and (b) real and (c) imaginary parts of the dielectric permittivity and of (d) the conductivity of the $\text{Pr}_{0.7}\text{Ca}_{0.3}\text{MnO}_3$ polycrystalline sample measured at various temperatures. Solid lines show the results of the least-squares fits of the measured infrared reflectivity spectra, together with the directly measured terahertz spectra (dots below 60 cm^{-1}) using expressions (1)–(3) (see the text). The dashed line in (d) corresponds to the frequency squared dispersion of the lowest-frequency infrared phonon “tail.”

form of three structured bands at 180 – 190 , 320 – 330 , and 560 cm^{-1} . The fine structure of the bands is due to lowered symmetry caused by lattice distortions resulting from the high-temperature phase transition from the cubic $Pm3m$ modification to the orthorhombic distorted perovskite $Pnma$ structure. After this phase transition the phonons from the R , M , X , and Γ points of the Brillouin zone obtain spectral activity as a result of the fourfold multiplication of the unit cell. The factor group analysis predicts 25 polar phonons of the $9B_{1u} + 7B_{2u} + 9B_{3u}$ symmetry. All these phonons are seen in our spectra and are fitted with Lorentzian terms. Below we concentrate mainly on the far-IR and THz frequency ranges where the charge carriers’ response is best pronounced.

The main temperature changes are observed in the reflectivity spectra at frequencies below 100 cm^{-1} . While cooling down, the reflectivity decreases and flattens out at the lowest temperature of 10 K. A similar behavior is observed for the real part of dielectric permittivity. Much stronger temperature variations are seen in the spectra of the imaginary part

of the dielectric permittivity $\varepsilon_2(\nu)$ and of the dynamical conductivity $\sigma(\nu)$ whose values change by almost two orders of magnitude when the samples are cooled from 200 to 10 K. The $\varepsilon_2(\nu)$ spectra reveal also qualitative changes: Here, the transformation of the frequency dispersion from a negative to positive slope is detected. In addition, at the lowest temperature, $T = 10$ K, the development of an absorption peak at around $40\text{--}60\text{ cm}^{-1}$ (energy $5\text{--}7.5\text{ meV}$) is reliably identified in all three samples. Its origin will be discussed later.

Let us analyze the strongly temperature-dependent dispersion seen in the spectra below $40\text{--}50\text{ cm}^{-1}$. The pronounced decrease towards high frequencies seen at high temperatures in the $\varepsilon_1(\nu)$ and $\varepsilon_2(\nu)$ spectra can be formally connected with three types of dispersion mechanisms: (i) first, a Debye-like relaxation [33] given by the complex permittivity

$$\varepsilon_{\text{rel}}^*(\nu) = \frac{\Delta\varepsilon_{\text{rel}}}{1 + i\omega\tau_{\text{rel}}}, \quad (1)$$

where $\Delta\varepsilon_{\text{rel}}$ is the strength of the relaxation, $\tau_{\text{rel}} = (2\pi\gamma_{\text{rel}})^{-1}$ is the relaxation time, γ_{rel} is the relaxation frequency, and $\omega = 2\pi\nu$ is the circular frequency. For $\nu > \gamma_{\text{rel}}$, both ε_1 and ε_2 decrease with frequency, as seen in the experiment. However, we do not consider this case since it corresponds to the zero dc conductivity σ_0 , in strong contrast to experimental observations that provide the values of $\sigma_0(200\text{ K}) \approx 0.3\text{--}2\ \Omega^{-1}\text{ cm}^{-1}$ for PCMO with $x = 0.3\text{--}0.5$; even larger values are obtained for thin films on various substrates [11,13,34–37]. (ii) The Mott-like hopping mechanism with $\sigma(\nu) \sim \nu^s$ ($s < 1$) and corresponding dispersions of $\varepsilon_1 \sim \nu^{1-s}$ and $\varepsilon_2 \sim \nu^{s-1}$ [33] also leads to the behavior observed in our THz spectra of ε_1 and ε_2 at not too low temperatures. However, to simultaneously fit the measured $\varepsilon_1(\nu)$, $\varepsilon_2(\nu)$, and $\sigma(\nu)$ spectra, one would need to use unphysically low values of the hopping exponent $s \approx 0.3\text{--}0.4$. (iii) We thus take the third case when the high-temperature spectral dispersion is connected with the response of free charge carriers given by the Drude expression for the complex conductivity [30,38]:

$$\sigma_{\text{Drude}}^*(\nu) = \frac{\sigma_0}{1 - i\nu/\gamma_D}, \quad (2)$$

where σ_0 is the dc conductivity and γ_D is the charge-carrier scattering rate. In the low-frequency limit, $\nu \ll \gamma_D$, expression (2) yields $\sigma(\nu) = \sigma_0 = \text{const}$, $\varepsilon_2 = 2\sigma(\nu)/\nu \sim 1/\nu$, and $\varepsilon_1 = \text{const}$. By fitting the THz spectra with expression (2) we obtain dc conductivity values that are in perfect accord with the literature data. (For the scattering rate only an estimate of $\gamma_D > 200\text{ cm}^{-1}$ is possible.) To account for the dispersion of the real part of the permittivity $\varepsilon_1(\nu)$, which is not reproduced by (2), we had to introduce one more term given by (1) whose origin is discussed below. (We note that using the combination of the hopping and the Drude terms for fitting the spectra still leads to unsatisfactory low values of the hopping exponent s and of the dc conductivity σ_0 .) Physically, the absence of any noticeable hopping contribution in the THz response in our case must be connected with the lower sensitivity of the reaction of the charge carriers to the probing THz radiation as compared to the dc case when the carriers suffer all possible imperfections, intrinsic and extrinsic, that impede/damp their motion and lead to localization (partial or

complete) and a corresponding hoppinglike response. Indeed, typical signatures of the hopping transport are really detected below the THz range—at radio-frequency ac experiments and in the dc cases [11,12,13,15,34–37,39,40]. We can conclude that with our THz radiation we probe intrinsic electrical properties of the studied compounds that are not corrupted by extrinsic defects.

To find out the temperature dependences of the parameters of the terms used to fit the obtained spectra and to analyze the underlying physics, the IR reflectivity spectra (upper frames in Figs. 2–4) were processed together with the directly measured THz $\varepsilon_1(\nu)$, $\varepsilon_2(\nu)$, and $\sigma(\nu)$ spectra using the least-squares method. The phonon peaks and the THz resonance that appears at low temperatures were modeled by standard Lorentzian expressions

$$\sigma^*(\nu) = \frac{0.5\Delta\varepsilon\nu_0^2\nu}{\nu\gamma + i(\nu_0^2 - \nu^2)}, \quad (3)$$

where $\Delta\varepsilon$ is the dielectric contribution, ν_0 is the resonance frequency, and γ is the damping constant. The fitting results are shown by the solid lines in Figs. 2–4. In Fig. 3, the three different mechanisms [relaxation term (1), free carrier Drude term (2), and the Lorentzian (3)] responsible for the

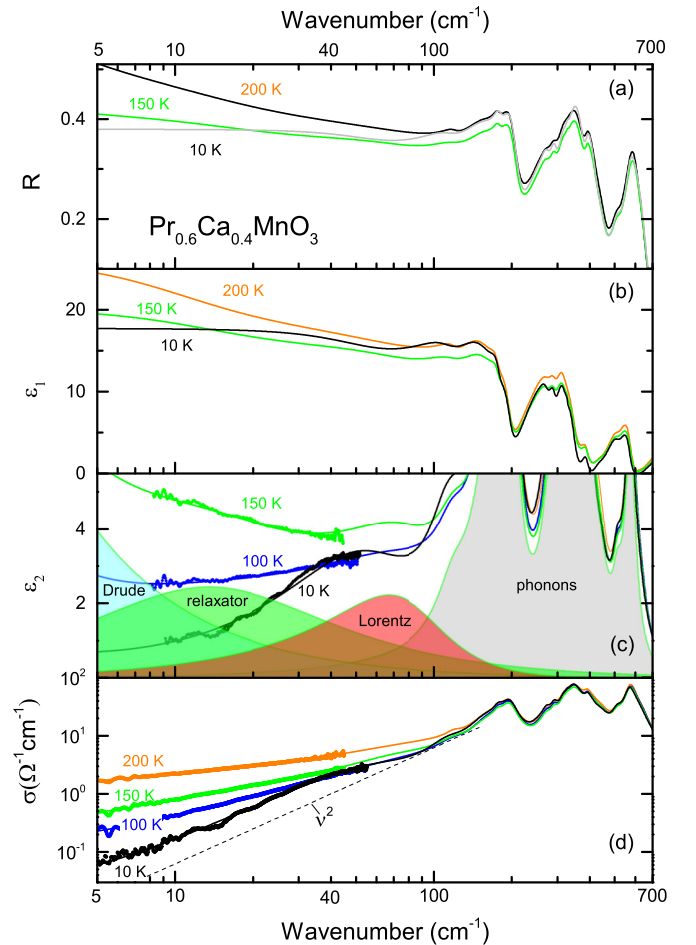


FIG. 3. Same as Fig. 2, for the $\text{Pr}_{0.6}\text{Ca}_{0.4}\text{MnO}_3$ polycrystalline sample with spectral contributions [expressions (1)–(3)] shown separately.

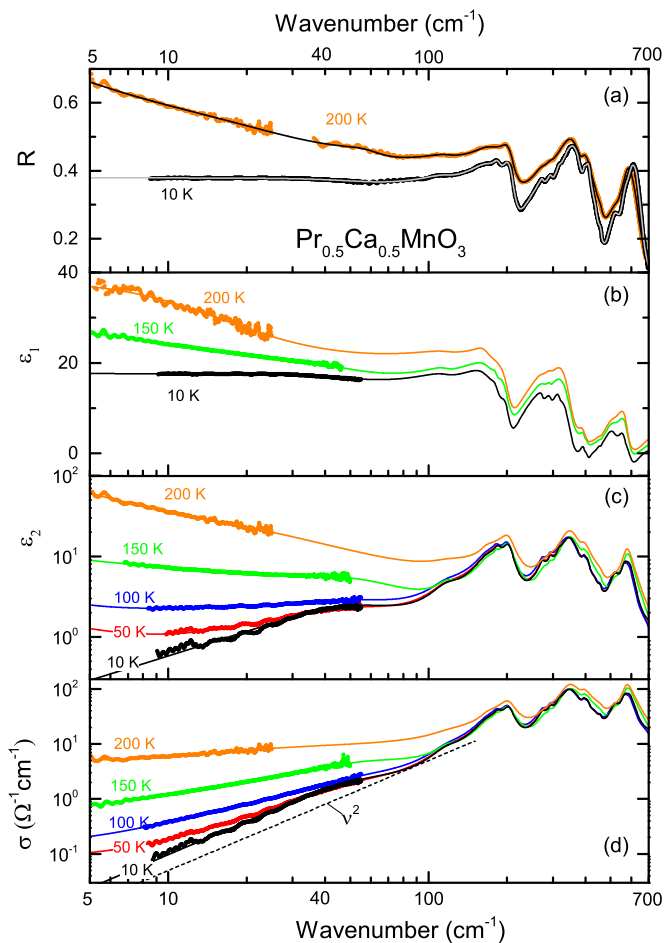


FIG. 4. Same as Fig. 2, for the $\text{Pr}_{0.5}\text{Ca}_{0.5}\text{MnO}_3$ polycrystalline sample.

dispersion at THz frequencies are shown separately for the $x = 0.4$ sample.

We first discuss the origin of the free carrier Drude term and the relaxational contributions. From our THz-IR data we are not able to clarify the nature of the itinerant charge carriers whose response is described by Drude expression (2). We just accept the common idea that these carriers in our $\text{Pr}_{1-x}\text{Ca}_x\text{MnO}_3$ samples are (small) polarons [11,12,41]. [The typical polaronic absorption edge is seen in our spectra (Fig. 5), in accordance with the published optical data [41,42].] However, we cannot associate the Drude-like response with the thermally assisted *hopping* of polarons since any hopping mechanism would imply a noticeable frequency dependence (growth) of the ac conductivity [33] as opposed to our analysis based on expression (2) that implies $\sigma(\nu) = \sigma_0 = \text{const}$. This leads us to the conclusion that the polaron dynamics is coherent and that they are moving within a band that can be 2.4–7.5 meV wide [35]. In Fig. 6(a) we plot the temperature variation of the conductivity σ_0 in an Arrhenius representation. Two regimes are clearly seen with the activation energies at high temperatures $E_a^{\text{HT}} = 95\text{--}140\text{ meV}$ and at low temperatures $E_a^{\text{LT}} = 2.6\text{--}4.3\text{ meV}$ determined according to $\sigma = ne\mu \sim \text{const} \exp(-E_a/k_B T)$ (here, n is the concentration of charge carriers with charge e and with mobility μ , and k_B is the Boltzmann constant). The crossover between the two regions

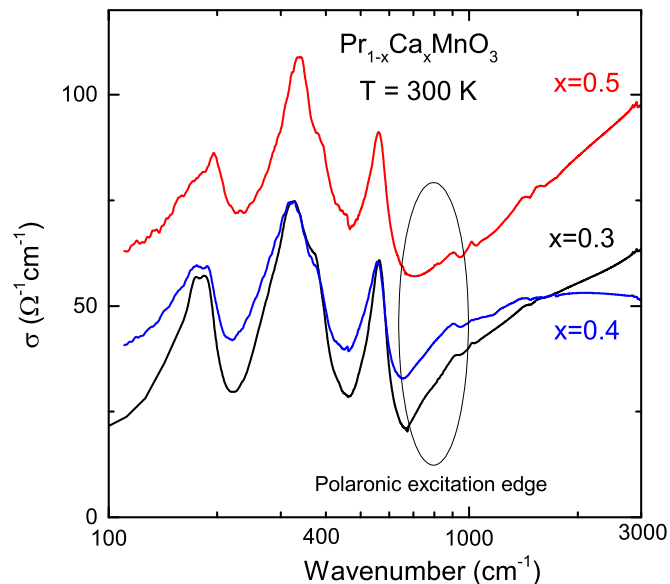


FIG. 5. Room-temperature infrared conductivity spectra of $\text{Pr}_{1-x}\text{Ca}_x\text{MnO}_3$ polycrystalline samples obtained by a Kramers-Kronig analysis of the reflectivity spectra. The onset of absorption due to polaronic excitation is shown with an oval.

falls in the range 120–170 K. At high temperatures, the value of E_a^{HT} agrees well with the model-independent determination of the onset absorption (charge gap) of 180 meV and of 120–160 meV seen in the optical conductivity and absorption spectra of single crystalline $\text{Pr}_{0.6}\text{Ca}_{0.4}\text{MnO}_3$ [42] and thin film $\text{Pr}_{0.64}\text{Ca}_{0.36}\text{MnO}_3$ [43] samples, respectively.

The activated behavior of the conductivity at high temperatures implies that it is governed mainly by the change in the carrier density n rather than in their mobility μ . This is in accordance with our interpretation of the relaxation peaks that are observed in $\epsilon_2(\nu)$ and $\sigma_1(\nu)$ spectra at THz frequencies in all three samples; in Fig. 3(c) such peaks are shown separately for the $x = 0.4$ compound. We associate the relaxation with the charge ordering process of the type similar to what is found in the dynamical response of the systems with order-disorder phase transitions. An example of such a response is given by ferroelectrics or dipolar glass relaxors [44] where the potential energy of the system is characterized by two or more minima [45,46]. At high temperatures, the minima are randomly occupied due to thermal disorder. During cooling down, the system components (dipoles in relaxors or charges in our case) try to go into the deepest minima to minimize the total potential energy. The dynamics of such a process is commonly described by a relaxation behavior of a certain response function (such as the dielectric permittivity or ac conductivity) with a single relaxation time $\tau_{\text{rel}} = (2\pi\gamma_{\text{rel}})^{-1}$ [expression (1)] or a distribution of relaxation times revealing definite temperature dependences [44]. We note that earlier we have observed this kind of relaxational excitation also in another manganite, $\text{La}_{0.25}\text{Ca}_{0.75}\text{MnO}_3$ ceramic [47], though with a significantly lower damping constant $\gamma < 5\text{ cm}^{-1}$ compared to the present PCMO compounds. In the present case the values of the damping are significantly larger and increase with cooling [Fig. 6(c)]. The dielectric contribution $\Delta\epsilon$ (the intensity) of the

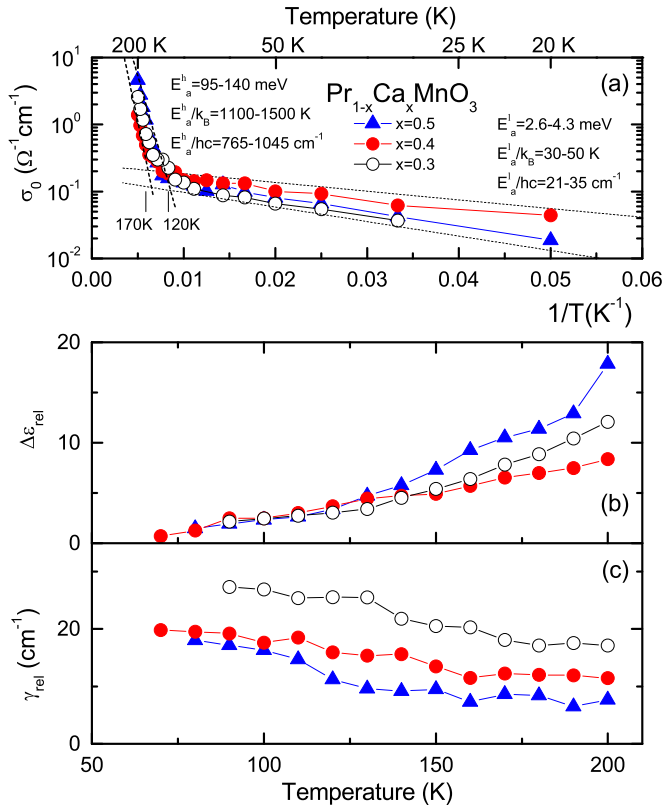


FIG. 6. (a) Arrhenius plot of the dc conductivity of $\text{Pr}_{1-x}\text{Ca}_x\text{MnO}_3$ polycrystalline samples obtained by least-squares fitting of the spectra presented in Figs. 2–4, as described in the text. The values of σ_0 correspond to the Drude term (2), whose spectral contribution is shown separately in Fig. 3(c). The dashed lines show ranges (indicated with numbers; h is the Planck’s constant, c is the speed of light) of activation energies describing the variations of conductivity at high (E_a^h) and low (E_a^l) temperatures. (b), (c) Temperature dependences of the parameters of the Debye relaxator term (1) [the spectral contribution is shown separately for $x = 0.4$ in Fig. 3(c)] and the dielectric contribution $\Delta\epsilon_{\text{rel}}$ and γ_{rel} obtained by least-squares fitting of the spectra presented in Figs. 2–4, as described in the text.

relaxation decreases towards low temperatures, indicating the decrease of charge-carrier density. The nature of the minima where the charges reside can be of extrinsic (defects and grain boundaries in the polycrystalline sample) or of some kind of intrinsic origin, such as localization on lattice distortions produced by Mn-O-Mn bond bending.

From Fig. 6 it is seen that the Drude term contributes to the THz spectra with measurable values of σ_0 for temperatures as low as 20 K, while the relaxation peak becomes unobservable below 70 K. A strong change in the activation energy is observed below 120–170 K. In the same temperature interval a well-defined shift to lower energies of the charge gap was detected in single crystalline $\text{Pr}_{0.6}\text{Ca}_{0.4}\text{MnO}_3$ for the polarization of the electric field E of the radiation parallel to the b axis, $E \parallel b$ [42]. The same tendency for the optical gap energy was deduced also from the absorptivity spectra of $\text{Pr}_{0.64}\text{Ca}_{0.36}\text{MnO}_3$ thin films [43]. In Ref. [42] it was concluded that the gap evolution in the b -polarized optical

spectra is governed by the magnetic ordering. Since the transition temperatures T_N to a magnetically ordered state in our three samples fall within the interval 120–170 K, we believe that the strong (by about 30 times—see Fig. 6) change of the activation energies and probably of the conduction mechanisms is connected to the onset of magnetic order. Since in manganites the spin subsystem strongly couples to the charge, orbital, and phonon degrees of freedom, the development of an antiferromagnetic order can stimulate overlapping of electronic wave functions and thus lead to increased transfer integrals and facilitation of charge transport.

Finally, we discuss the origin of the THz resonance. We believe that it is connected with the coupling to phonons of the electrons of the f shell of the Pr^{3+} ion. The electronic configuration of the trivalent praseodymium is $\text{Pr}^{3+}(4f^2)$. In the crystal, ionic J levels are split into Stark components. The $4f^2$ electronic configuration of the Pr^{3+} ion generates four singlet (1S_0 , 1D_2 , 1G_4 , 1I_6) and nine triplet (3M_4 , 3M_5 , 3M_6 , 3F_2 , 3F_3 , 3F_4 , 3P_0 , 3P_1 , 3P_2) terms with the 3M_4 term corresponding to the ground state [48]. The higher-energy terms are 3M_5 , 3M_6 , 3F_2 , 3F_3 , 3F_4 , 1G_4 and the transition energies between the terms correspond to infrared frequencies. In the case of PrMnO_3 , which is symmetrically analogous to the solid solutions studied in the present work, the splitting of the three lowest-energy levels was calculated in Ref. [49]. For the term 3M_4 ($i = 1\text{--}9$), the nine corresponding components are located at frequencies 7, 19, 59, 110, 138, 270, 309, 515, and 718 cm^{-1} ; for 3M_5 the 11 components fall in the range $2146\text{--}2676\text{ cm}^{-1}$; the term 3M_6 is split into 13 components lying in the range $4197\text{--}4982\text{ cm}^{-1}$. Similar results with slightly lower splitting energies were obtained in a recent paper [50] within the approach based on local Hamiltonian and Wannier function calculations. One of the interlevel transitions—between the 7 and 19 cm^{-1} terms ($\Delta\epsilon_{\text{CF}} \approx 13\text{ cm}^{-1}$)—was experimentally observed in Ref. [51].

Since the f shell of the RE^{3+} ions is filled, their electronic states are only weakly affected by the ligand crystal field changes. Nevertheless, phonons can play a noticeable role in determining the energetics of the RE ions due to these ions’ interactions with the dynamical component of the crystal field (phonons). This leads to the involvement of phonons in the processes of nonradiative relaxation of electronic energy of the RE ion [52]. Phonons can even be observed in the optical spectra of impurity RE-ion-phonon interactions [53]. In some cases, in the optical spectra, a weak phonon wing can be detected that accompanies the narrow phononless RE impurity absorption line [53]. Such phonon wing appears due to a linear electron-phonon interaction of the impurity ion, and this can be termed as vibronic excitation. Its intensity is determined by the phonons density of states $g(\nu)$ and by the electron-phonon coupling constant L_q [53]: $I \sim L_q^2 g(\nu) \nu^{-1}$. The vibronic spectral shape depends on the details of the vibrational states of ligands in the vicinity of the RE center and on the specificity of the electron-phonon interaction between the ion and the crystal field. Some details on the dependence of vibronic transitions between the RE electronic states on covalent bonding between the impurity and ligand ions and on the type of the RE ion are discussed in Refs. [54,55]. We assign the resonance seen at $40\text{--}60\text{ cm}^{-1}$ in the THz spectra of $\text{Pr}_{1-x}\text{Ca}_x\text{MnO}_3$ to the

absorption of the THz radiation due to the vibronic transition in the system “RE-ion+ligand” where the Pr^{3+} electronic transitions between the 3M_4 ($i = 1-9$) terms are coupled to the acoustical phonon branches. According to our results, the intensity of the THz resonance does not noticeably depend on the Pr ion content, in the range $x(\text{Pr}) = 0.5-0.7$. It is unlikely that such variations of $x(\text{Pr})$ can cause significant changes of the electron-phonon coupling constant L_q that enters the above expression for the vibronic absorption. We thus assume that the observed effect is mainly associated with the fact that the acoustic phonon density of states $g(\nu)$ is formed by all ions within the unit cell of the compounds with the role of the Pr ion being not appreciable, thus keeping the intensity of the THz absorption line practically independent on $x(\text{Pr})$.

In conclusion, by using cw and pulsed terahertz spectroscopy techniques and infrared Fourier-transform spectroscopy, the broadband ($5-3000\text{ cm}^{-1}$) spectra of conductivity and dielectric permittivity are measured at temperatures 10–300 K of the polycrystalline manganites $\text{Pr}_{1-x}\text{Ca}_x\text{MnO}_3$ with $x = 0.3, 0.4, \text{ and } 0.5$. Three spectral components are revealed at terahertz frequencies that correspond to the Drude-

like response of free charge carriers, to the resonance centered at $40-60\text{ cm}^{-1}$, and to relaxational dispersion around $10-20\text{ cm}^{-1}$. The Drude component is assigned to the bandlike response of small polaronic charge carriers. It is shown that the amplitude of this free carrier conductivity is thermally activated with the activation energy changing from 95 to 140 meV above 120–170 K to 2.6–4.3 meV at lower temperatures. The temperature driven crossover is associated with setting in of the magnetic order. The nature of the terahertz resonance at $40-60\text{ cm}^{-1}$ is assigned to the transition between Stark-split Pr^{3+} electron states that gain optical activity due to coupling to acoustical phonons. The relaxation at $10-20\text{ cm}^{-1}$ is caused by delocalized polarons whose response is governed by their dynamics in presence of random localizing potential.

ACKNOWLEDGMENTS

The study was funded by Russian Ministry of Education and Science (Program 5 top 100) and by RFBR according to the Research Project No. 16-32-00739 MOJI_a. We thank G. Untereiner for technical help and sample preparation.

-
- [1] M. Uehara, S. Mori, C. H. Chen, and S.-W. Cheong, *Nature (London)* **399**, 560 (1999).
- [2] L. Zhang, C. Israel, A. Biswas, R. L. Greene, and A. de Lozanne, *Science* **298**, 805 (2002).
- [3] J. M. D. Coey, M. Viret, and S. von Molnar, *Adv. Phys.* **48**, 167 (1999).
- [4] C. N. R. Rao, A. R. Raju, V. Ponnambalam, S. Parashar, and N. Kumar, *Phys. Rev. B* **61**, 594 (2000).
- [5] M. Tokunaga, N. Miura, Y. Tomioka, and Y. Tokura, *Phys. Rev. B* **57**, 5259 (1998).
- [6] V. Kiryukhin, D. Casa, J. P. Hill, B. Keimer, A. Vigliante, Y. Tomioka, and Y. Tokura, *Nature (London)* **386**, 813 (1997).
- [7] Y. Moritomo, H. Kuwahara, Y. Tomioka, and Y. Tokura, *Phys. Rev. B* **55**, 7549 (1997).
- [8] D. Emin, *Phys. Rev. B* **48**, 13691 (1993).
- [9] Ch. Hartinger, F. Mayr, J. Deisenhofer, A. Loidl, and T. Kopp, *Phys. Rev. B* **69**, 100403(R) (2004).
- [10] Ch. Hartinger, F. Mayr, A. Loidl, and T. Kopp, *Phys. Rev. B* **73**, 024408 (2006).
- [11] C. Jooss, L. Wu, T. Beetz, R. F. Klie, M. Beleggia, M. A. Schofield, S. Schramm, J. Hoffmann, and Y. Zhu, *Proc. Natl. Acad. Sci. USA* **104**, 13597 (2007).
- [12] C. C. Wang and L. W. Zhang, *New J. Phys.* **9**, 210 (2007).
- [13] V. G. Prokhorov, G. G. Kaminsky, V. S. Flis, and Y. P. Lee, *Low Temp. Phys.* **25**, 792 (1999).
- [14] G.-m. Zhao, H. Keller, and W. Prellier, *J. Phys.: Condens. Matter* **12**, L361 (2000).
- [15] J. Sichelschmidt *et al.*, *Eur. Phys. J. B* **20**, 7 (2001).
- [16] S. Fratini and S. Ciuchi, *Phys. Rev. Lett.* **91**, 256403 (2003).
- [17] K. H. Kim, J. H. Jung, and T. W. Noh, *Phys. Rev. Lett.* **81**, 1517 (1998).
- [18] A. M. L. Lopes, J. P. Araujo, V. S. Amaral, J. G. Correia, Y. Tomioka, and Y. Tokura, *Phys. Rev. Lett.* **100**, 155702 (2008).
- [19] N. Kida and M. Tonouchi, *Phys. Rev. B* **66**, 024401 (2002).
- [20] R. Rana, N. Awari, P. Pandey, A. Singh, S. S. Prabhu, and D. S. Rana, *J. Phys.: Condens. Matter* **25**, 106004 (2013).
- [21] A. Nucara, P. Maselli, P. Calvani, R. Sopracase, M. Ortolani, G. Gruener, M. Cestelli Guidi, U. Schade, and J. García, *Phys. Rev. Lett.* **101**, 066407 (2008).
- [22] J. Fujioka, Y. Ida, Y. Takahashi, N. Kida, R. Shimano, and Y. Tokura, *Phys. Rev. B* **82**, 140409(R) (2010).
- [23] N. Biškup, A. de Andrés, J. L. Martinez, and C. Perca, *Phys. Rev. B* **72**, 024115 (2005).
- [24] R. S. Freitas, J. F. Mitchell, and P. Schiffer, *Phys. Rev. B* **72**, 144429 (2005).
- [25] Z. Jirak, S. Krupicka, Z. E. Simsa, M. Dlouha, and S. Vratilav, *J. Magn. Magn. Mater.* **53**, 153 (1985).
- [26] H. Yoshizawa, H. Kawano, Y. Tomioka, and Y. Tokura, *Phys. Rev. B* **52**, R13145(R) (1995).
- [27] Y. Tomioka, A. Asamitsu, H. Kuwahara, Y. Moritomo, and Y. Tokura, *Phys. Rev. B* **53**, R1689(R) (1996).
- [28] R. K. Zheng, G. Li, Y. Yang, A. N. Tang, W. Wang, T. Qian, and X. G. Li, *Phys. Rev. B* **70**, 014408 (2004).
- [29] B. Gorshunov, A. Volkov, I. Spektor, A. Prokhorov, A. Mukhin, M. Dressel, S. Uchida, and A. Loidl, *Int. J. Infrared Millimeter Waves* **26**, 1217 (2005).
- [30] M. Dressel and G. Gruner, *Electrodynamics of Solids* (Cambridge University Press, Cambridge, UK, 2002).
- [31] T. Elovaara, H. Huhtinen, S. Majumdar, and P. Paturi, *J. Phys.: Condens. Matter* **24**, 216002 (2012).
- [32] E. Pollert, S. Krupicka, and E. Kuzmicova, *J. Phys. Chem. Solids* **43**, 1137 (1982).
- [33] A. K. Jonscher, *Dielectric Relaxation in Solids* (Chelsea Dielectric Press, London, 1983).
- [34] Z. Sheng, M. Nakamura, F. Kagawa, M. Kawasaki, and Y. Tokura, *Nat. Commun.* **3**, 944 (2012).
- [35] J. Hoffmann, P. Moschkau, S. Mildner, J. Norpoth, C. Jooss, L. Wu, and Y. Zhu, *Mater. Res. Express* **1**, 046403 (2014).

- [36] M. Staruch, L. Stan, J. H. Lee, H. Wang, J. I. Budnick, and M. Jain, *J. Appl. Phys.* **110**, 013921 (2011).
- [37] A. Pimenov, M. Biberacher, D. Ivannikov, A. Loidl, A. A. Mukhin, Y. G. Goncharov, and A. M. Balbashov, *Phys. Rev. B* **73**, 220407(R) (2006).
- [38] A. V. Sokolov, *Optical Properties of Metals* (Elsevier, New York, 1967).
- [39] S. Yamada, T. Arima, and K. Takita, *J. Phys. Soc. Jpn.* **68**, 3701 (1999).
- [40] A. Levstik, C. Filipič, V. Bobnar, A. Potočnik, D. Arčon, S. Drnovšek, J. Holc, and Z. Jagličić, *Phys. Rev. B* **79**, 153110 (2009).
- [41] S. Mildner, J. Hoffmann, P. E. Blöchl, S. Teichert, and C. Jooss, *Phys. Rev. B* **92**, 035145 (2015).
- [42] Y. Okimoto, Y. Tomioka, Y. Onose, Y. Otsuka, and Y. Tokura, *Phys. Rev. B* **59**, 7401 (1999).
- [43] G. Saucke, J. Norpoth, C. Jooss, D. Su, and Y. Zhu, *Phys. Rev. B* **85**, 165315 (2012).
- [44] B. Z. R. Blinc, *Soft Modes in Ferroelectrics and Antiferroelectrics* (North-Holland, Amsterdam, 1974).
- [45] N. F. Mott, *Metal-Insulator Transitions*, 2nd ed. (Taylor & Francis, London, 1990).
- [46] N. F. Mott and E. A. Davis, *Electronic Processes in Non-crystalline Solids* (Oxford University Press, London, 1971).
- [47] T. Zhang, E. Zhukova, B. Gorshunov, D. Wu, A. S. Prokhorov, V. I. Torgashev, E. G. Maksimov, and M. Dressel, *Phys. Rev. B* **81**, 125132 (2010).
- [48] W. H. Flygare, *Molecular Structure and Dynamics* (Prentice Hall, Englewood Cliffs, NJ, 1978).
- [49] S. Jandl, V. Nekvasil, A. A. Mukhin, and M. L. Sadowski, *J. Magn. Magn. Mater.* **311**, 583 (2007).
- [50] P. Novak, V. Nekvasil, and K. Knizek, *J. Magn. Magn. Mater.* **358–359**, 228 (2014).
- [51] A. A. Mukhin, V. Y. Ivanov, V. D. Travkin, and A. M. Balbashov, *J. Magn. Magn. Mater.* **226–230**, 1139 (2001).
- [52] I. S. Osad'ko, *Phys. Rep.* **206**, 43 (1991).
- [53] W. M. Yen, W. C. Scott, and A. L. Schawlow, *Phys. Rev.* **136**, A271 (1964).
- [54] C. de Mello Donega, M. J. D. Crombag, A. Meijerink, and G. Blasse, *J. Lumin.* **60–61**, 74 (1994).
- [55] A. Ellens, S. Schenker, A. Meijerink, and G. Blasse, *J. Lumin.* **72–74**, 183 (1997).